Chemical Engineering Journal 378 (2019) 122132

Contents lists available at ScienceDirect

Chemical Engineering Journal

journal homepage: www.elsevier.com/locate/cej

Sulfur doped carbon quantum dots loaded hollow tubular g-C_3N_4 as novel photocatalyst for destruction of *Escherichia coli* and tetracycline degradation under visible light

Wenjun Wang[a,1], Zhuotong Zeng[b,1], Guangming Zeng[a,*], Chen Zhang[a,*], Rong Xiao[b,*], Chengyun Zhou[a], Weiping Xiong[a], Yang Yang[a], Lei Lei[a], Yang Liu[a], Danlian Huang[a], Min Cheng[a], Yaya Yang[a], Yukui Fu[a], Hanzhuo Luo[a], Yin Zhou[a]

[a] College of Environmental Science and Engineering, Hunan University and Key Laboratory of Environmental Biology and Pollution Control (Hunan University), Minisy of Education, Changsha 410082, PR China
[b] Department of Dermatology, Second Xiangya Hospital, Central South University, Changsha 410011, PR China

HIGHLIGHTS

- Novel S-CQDs/hollow tubular g-C_3N_4 photocatalyst was successfully fabricated.
- HTCN-C(2) exhibited excellent photocatalytic activity for *Escherichia coli* photodestruction.
- The changes of *Escherichia coli* morphology and inside contents were verified by SEM images.
- h^+, $^{\cdot}O_2^-$ and $^{\cdot}OH$ radicals participate in the photocatalytic degradation process.
- Cycle experiments revealed the outstanding photo-stability and reusability.

GRAPHICAL ABSTRACT

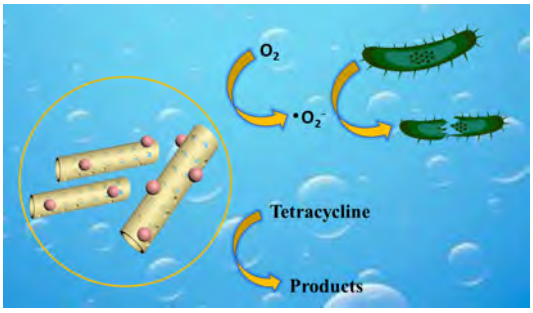

ARTICLE INFO

Keywords:
Hollow tubular g-C_3N_4
Bacterial destruction
Photocatalytic
Modified CQDs

ABSTRACT

Microbial contamination and antibiotic pollutions diffusely exist in wastewater system, and contaminated water poses a threat to public health. Therefore, there is a need to effectively remove biohazard and antibiotic contamination from wastewater systems. In this paper, sulfur doped carbon quantum dots (S-CQDs)/hollow tubular g-C_3N_4 photocatalyst (HTCN-C), prepared via ultrasonic assisted synthesis strategy, was regarded as an efficient catalyst for the degradation of antibiotic (tetracycline) and destruction of a typical Gram-negative bacterium (*Escherichia coli*) in imitated wastewater system. The unique structures of hollow tubular g-C_3N_4 and loading of modified carbon quantum dots enhanced electron transfer and charge separation, leading to a significant improvement in photocatalytic efficiency. Benefiting from these merits, the optimized catalysts (HTCN-C(2)) exhibited superior performance with a reaction rate of 0.0293 min^{-1} for tetracycline (TC) degradation and 99.99% destruction of *Escherichia coli* under visible-light irradiation. Moreover, the characterization of UV–Vis diffuse reflectance spectra, photoluminescence technique, transient photocurrent responses and electrochemical impedance spectroscopy also verified the good optical and electrochemical properties of resultant samples. Our current work indicates that HTCN-C has great potential in degradation of antibiotic and destruction of bacterium for practical wastewater treatment.

* Corresponding authors at: College of Environmental Science and Engineering, Hunan University, Changsha 410082, PR China.
E-mail addresses: zgming@hnu.edu.cn (G. Zeng), zhangchen@hnu.edu.cn (C. Zhang), xiaorong65@csu.edu.cn (R. Xiao).
[1] These authors contribute equally to this article.

https://doi.org/10.1016/j.cej.2019.122132
Received 1 April 2019; Received in revised form 24 June 2019; Accepted 1 July 2019
Available online 02 July 2019

1. Introduction

The rapid development of economic has brought convenience to people in recent years, while it has also brought many serious environmental problems [1–5]. Due to the infectious waterborne diseases of biohazards and poor biodegradability of antibiotic, microbial contaminations and antibiotic pollutions were unwanted constituents in water system [6–10]. For example, *Escherichia coli*, as a pathogenic microorganism, can cause a variety of intestinal diseases. The existence of tetracycline (TC) can also lead to antibiotic resistance problem [11–13]. Therefore, finding an effective way to remove these contaminants in wastewater is of great importance [14–16]. However, there exist huge challenges and difficulties to effective elimination of these contaminants [17–19]. Conventional wastewater disinfection methods such as ultraviolet irradiation, microbial degradation, chlorination, and ozonation have been proposed and obtained good improvement, but their applications are limited due to the high energy consumption, noxious disinfection by-products, enormous cost, and complex process [20–23].

Very recently, semiconductor photocatalytic technique has attracted considerable attention in organic pollutants elimination, bacterial disinfection and energy generation for their non-byproducts, powerful photocatalytic ability, environment friendly and cost-effective advantages [24,25]. Based on previous studies, it was vital to choose a "suitable" photocatalyst in the process of photocatalysis [26,27]. The practical applications of traditional photocatalysts (ZnO, SnO_2, and TiO_2) were restricted by their low solar-energy utilization efficiency, wide band-gap, and high recombination rate of light induced e^-/h^+ [28,29]. Non-metal graphitic carbon nitride (g-C_3N_4), a fascinating organic semiconductor photocatalyst, has a great deal of advantages including reliable chemical inertness, appealing optical characteristics, excellent thermal stability, and proper band-gap, making it particularly suitable for applications in organic synthesis, bacterial disinfection, energy conversion and elimination of organic pollutants [30]. However, owing to the sluggish exciton dissociation, insufficient light absorption and low practical surface area, the photocatalytic activity of bulk g-C_3N_4 needs to be further enhanced [31]. Hence, different strategies such as morphological engineering, combination with conductive materials, element doping and constructing vacancy defects have been proposed to address these intrinsic drawbacks [32]. Photocatalytic processes generally occur on the surface of the photocatalysts, so the modified g-C3N4 with nanostructures and unique morphology exhibit superior optical and chemical properties than their bulk counterparts. To date, various nanostructure morphologies (ribbons, sheets, tubes, fibers, rods, wires, particles, spheres, etc.) of g-C_3N_4 photocatalysts have been successfully prepared. According to recent experimental and theoretical studies, one-dimensional (1D) g-C_3N_4 nanotubes have drawn tremendous attention due to their unique structure, which possess high surface photocatalytic efficiency, facilitated electron transfer rate and excellent optical properties [33–35]. The aforesaid g-C_3N_4 nanotubes can be synthesized by liquid-phase reactions, wet-chemical routes, and template-assisted processes [36]. However, these mentioned methods were not intrinsically controllable because of the condition of high pressure, various organic additives, and indelible template residues. Thus, a facile method to synthesis tubular g-C_3N_4 with large scale is highly desirable.

Carbon quantum dots (CQDs), as a carbon-based material, are particularly encouraging because of their robust chemical inertness, good biocompatibility, low toxicity and excellent optical properties. In the field of photocatalysis, CQD acts as a photosensitizer and an electron mediator to broaden photon absorption region and decrease photo-induced e^-/h^+ recombination [37]. Moreover, CQDs also exhibit upconversion properties. Several semiconductors photocatalysts such as Bi_2WO_6, TiO_2, g-C_3N_4, $BiVO_4$, and ZnO can be coupled with CQDs to enhance their photocatalytic efficiency, which were attributed to a longer visible light absorption region, more charge carriers, and higher electron–hole pair separation [37–41]. According our group previous work, we reported a facile hydrothermal strategy for fabricating a novel 0D CQDs coupled 2D Bi_2WO_6 nanosheets composite nanomaterials (denoted as CBW) [38]. The CBW heterostructures exhibited better photocatalytic performance towards degradation of bisphenol A and methylene orange than pure 2D Bi_2WO_6 under the irradiation of visible and near-infrared light. Based on density functional theory (DFT) and experimental results, the valence band-edge hybridization and complementary conduction between pure 2D Bi_2WO_6 and CQDs could greatly enhance the electron–hole pair separation of CBW composite nanomaterials. Hence, loading CQDs on a semiconductor photocatalyst was vital for improving its photocatalytic efficiency. Moreover, heteroatom S doping was introducted into carbonaceous material to enhance its electrical conductivity and optical properties, which accelerates the electron transport and produces good catalytic performance [39,42,43].

Motivated by the above considerations, we used a simple ultrasonic-assisted method for the fabrication of modified CQDs loaded hollow tubular g-C_3N_4 novel photocatalyst (HTCN-C). In the first place, hollow tubular g-C_3N_4 was prepared via a molecule self-assembly between melamine and cyanuric acid. Then, a facile ultrasonic-assisted method was used to obtain HTCN-C (the detail procedures were proposed in Scheme 1 and supporting information). Notably, S-CQDs acted as a photosensitizer and an electron mediator to broaden photon absorption

Scheme 1. Schematic illustration of the preparation for modified carbon quantum dots loaded hollow tubular carbon nitride (HTCN-C) samples.

region and decrease photo-induced e^-/h^+ recombination in this system. The unique structures of hollow tubular g-C_3N_4 and loading of modified carbon quantum dots enhanced electron transfer and charge separation, leading to a significant improvement for the photo-destruction of a typical Gram-negative bacterium (*Escherichia coli*) and photo-degradation of TC in wastewater system. Our current study might shed light on fabricating of 0D/1D novel g-C_3N_4-based photocatalyst with advanced nanostructure for visible light utilization in bacteria destruction and pollutant degradation.

2. Experimental section

2.1. Reagents

Urea ($CO(NH_2)_2$), Melamine ($C_3N_3(NH_2)_3$), ethanol (E), tertiary butanol (TBA), 4-hydroxy-2,2,6,6-tetramethylpiperidinyloxy (TEMPOL), cyanuric acid, disodium ethylenediaminetetraacetate (EDTA-2Na), citric acid, acetone, Eosin Methylene Blue Agar, glutaraldehyde, l-cysteine and tetracycline (TC) were purchased from Sinopharm Corporation Ltd. (Shanghai, China). All materials or chemicals applied in this study were of analytical grade without additional purification.

2.2. Synthesis of the catalysts

The S-CQDs solution was obtained according to previous work with minor modifications [42]. To synthesize S-CQDs, 0.9607 g of citric acid (5 mmol) and 0.6058 g of l-cysteine (5 mmol) was dissolved in 5 mL of distilled water, respectively. The above solution was mixed and stirred 30 min. Subsequently, the resulting suspension was transferred to a 50 mL Teflon-lined stainless autoclave and kept for 6 h at 200 °C. Next, the final product was subjected to dialysis for 12 h for getting the purified S-CQDs solution. The diameter, the flattening width and the molecular weight cut off of the dialysis bag were 22 mm, 34 mm and 3500 Da, respectively.

Pristine g-C_3N_4 were synthesized according to our previous work [44]. The detailed procedures for preparing hollow tubular g-C_3N_4 were shown in the supporting information. As for preparing S-CQDs/hollow tubular g-C_3N_4 hybrids (HTCN-C), 0.2 g of hollow tubular g-C_3N_4 was scattered in 30 mL of distilled water. Subsequently, a certain volume (0.5, 1, 2, and 3 mL) of S-CQDs solution (0.1 mg/mL) was injected into above suspension. The mixture was subsequently sonicated 1 h and stirred 1 h, and then vacuum dried at 85 °C for 20 h to remove the liquid. Moreover, the procedures of synthesized S-CQDs/hollow tubular g-C_3N_4 photocatalysts were proposed in Scheme 1. The final photocatalysts was marked as HTCN-C(x), where x represents the S-CQDs volume. In addition, a summary table reporting all prepared catalyst was displayed in Table S1 to make it easier to understand the preparation process.

2.3. Characterization

The X-ray diffraction (XRD) patterns of as-obtained samples were recorded on a D/max-2500 Advance X-ray diffractometer with Cu Kα radiation. The functional groups of resultant samples were detected by Fourier transform infrared (FT-IR, Bruker Vertex 70) spectrophotometer with KBr pellet method. The X-ray photoelectron spectroscopy (XPS) was acquired on Escalab 250Xi instrument with an Al Kα X-ray source. Transmission electron microscopy (TEM) and Scanning electron microscopy (SEM) images were used to determine the morphology and microstructure of the nanomaterials. The photoluminescence (PL) spectra and UV–vis absorption (DRS) spectra were detected on a Fluromax-4 spectrofluorometer and Cary 300 UV–vis spectrophotometer, respectively. The FLS980 fluorescence spectrometer (excitation wavelength: 340 nm) was used to record time-resolved transient PL decay spectra. Total organic carbon (TOC) was detected on a Shimadzu TOC-LCPH analyzer. ESR signals of $^{\cdot}OH$ and $^{\cdot}O_2^-$ radicals were determined by a JEOL JES-FA200 spectrometer under the irradiation of visible light.

2.4. Evaluation of photocatalytic properties

2.4.1. Photocatalytic degradation activity

Under visible light irradiation, the resultant samples were employed to degrade TC (20 mg/L) to study their photocatalytic activities. The visible light source was provided by a PLS-SXE 300 W Xenon lamp, and its light density parameter was 0.33 W/cm^2. Furthermore, the photocatalytic reaction system and the emission spectrum of the visible light was presented in Fig. S1. Typically, the catalyst dosage was 1 g/L. Before the photocatalytic procedure, the solid-liquid system was churned for 60 min in the dark to achieve the adsorption–desorption equilibrium. The reaction TC suspension (2 mL) was taken out at a given interval time and filtered using a 0.45 μm membrane filter, and then analyzed by a Shimadzu UV-2700 spectrophotometer to record the concentration of TC (357 nm). The used photocatalyst was collected and rinsed several times with ultrapure water and ethanol to remove surface inclusions for next use, and five successive cycles of experiments were performed for TC degradation.

2.4.2. Photocatalytic disinfection capability

In addition, the bacterial disinfection activities of the resultant photocatalysts were estimated by using gram-negative strain *Escherichia coli* (*E. coli*) as a model bacterium. Before each experiment, all the glassware and Eosin Methylene Blue Agar were sterilized by an autoclave at 121 °C for 20 min. The cell density of the *E. coli* suspension was $\sim 3.0 \times 10^9$ colony forming units per milliliter (CFU/mL). Typically, 30 mg of HTCN-C was added into 49.5 mL of sterile water with the condition of ultrasonication. Next, the final viable cell density was changed to 3.0×10^7 CFU/mL since 0.5 mL of bacterial stock solution was dispersed in the above suspension. Similar to photo-degradation of TC, the suspension was also churned for 1 h in the dark to reach the adsorption-desorption equilibrium. 100 μL of the aliquot samples were collected and diluted at given time intervals (10 min), and then spread on Eosin Methylene Blue Agar plate. All photocatalytic bacterial inactivation experiments were carried out triplicate, and the data shown were the average of these triplicates. Then, above plates were incubated at 37 °C for 20 h to measure the viable cell density. Besides, the control experiments and blank reaction were carried out without photocatalysts and without light irradiation under the same condition, respectively.

2.5. Electrochemical measurements

CHI 660D electrochemical workstation was employed to record photocurrent density (PC), Mott-Schottky curve, and electrochemical impedance spectroscopy (EIS) of the resultant samples in a conventional three-electrode cell. The Ag/AgCl electrode and Pt electrode were served as reference electrode and counter electrode, respectively. And the prepared HTCN-C on 1 cm × 2 cm fluorine-doped tin oxide (FTO) glass were regarded as the working electrodes. In this typical experimental, light source was a 300 W Xeon lamp. And the electrolyte solution was 0.2 M of Na_2SO_4 liquid. Under the condition of room temperature, all the electrochemical measurements were obtained without bias potential.

3. Results and discussion

3.1. Structural characterization

The XRD patterns in Fig. 1a presented crystal phase structures of the samples of bulk g-C_3N_4, HTCN, and HTCN-C(x), x = 0.5, 1, 2 and 3. Consistent with the previous studies [45,46], a stronger diffraction peak at ~27.4° and a weaker one at ~13.1° were found from XRD patterns of

all the resultant samples, which were well indexed to g-C_3N_4 (JCPDS No. 87-1526). And the XRD pattern of pure S-CQDs was shown in Fig. S2. The peak at ~27.4° (0 0 2 peak) was assigned to the stacking of conjugated aromatic system with an interlayer distance of 0.34 nm. However, the weaker one at ~13.1° (1 0 0 peak) was assigned to in-plane structural packing motif of the tri-s-triazine units with a distance of 0.68 nm. There was no obvious difference with bulk g-C_3N_4, HTCN, and HTCN-C(x), manifesting that hollow tubular structure and the loading of S-CQDs did not affect the crystal structure of pure g-C_3N_4 in the preparation process. In addition, no additional peaks for S-CQDs were obtained might because of its poor crystallinity and limited amount in the composite [39,47]. It was worth noticing that 27.4° diffraction peak slightly shifted with increasing of S-CQDs (Fig. S3). The reason for this phenomenon was that S-CQDs adjusted the distance of layers, reflecting that S-CQDs was not limited to the shallow surface and the existence of strong interfacial interaction between the S-CQDs and g-C_3N_4 [37,48]. Furthermore, the loading of hollow tubular g-C_3N_4 by S-CQDs was also proved by organic elemental analysis results (Table S2). Compared to the C/N molar ratio (0.6517) of bulk g-C_3N_4, the higher C/N molar ratio (0.6959) of HTCN-C(2) and the content of sulfur element suggested the presence of S-CQDs.

It was easy to find that the samples of bulk g-C_3N_4, HTCN, and HTCN-C(x), x = 0.5, 1, 2 and 3 showed the similar framework in the typical FT-IR spectra (Fig. 1b). And FT-IR spectrum of pure S-CQDs was shown in Fig. S4. The typical characteristic peaks of g-C_3N_4 could be found in all photocatalysts, but the peaks of S-CQDs were scarcely obtained in resultant samples. This phenomenon suggested that the amount of S-CQDs was low and the loading of S-CQDs did not distinctly change the integral structure of pristine g-C_3N_4. As depicted in Fig. 1b, several major vibration bands at 3000–3500 cm^{-1} might be attributed to the surface adsorbed hydroxyl species (C—OH) and free amino groups (N—H). Vibrations bands ranging from 1100 to 1700 cm^{-1} belongs to the distinctive stretch modes of C—N heterocycles and the band at about 808 cm^{-1} was consistent with the particular signal of triazine unit [47]. In addition, a slight peak at ~1135 cm^{-1} corresponded to C—S and C—O bonds, which could be regarded as the indirect evidence that S-CQDs/hollow tubular g-C_3N_4 hybrids were successfully synthesized (Fig. S5).

The morphology and microstructure of bulk g-C_3N_4, HTCN and HTCN-C(2) were checked by SEM, and the consistent results were showed in Fig. 2. As depicted in Fig. 2a, bulk g-C_3N_4 prepared from direct calcination of melamine presented an aggregated and chunky structure [33]. In contrast, the as-obtained HTCN and HTCN-C(2) mainly displayed a well-developed hollow tubular morphology (Fig. 2b and Fig. 2c). The TEM measurement was introduced to further study the internal structure of bulk g-C_3N_4, HTCN and HTCN-C(2), and the pictures were shown in Fig. 3. The bulk g-C_3N_4 revealed as numerous ultrathin nanosheets with no pores (Fig. 3a). Fig. 3b and c verified that the embellished carbon nitride possessed hollow tubular structure with abundant of pores, which was in consistent with the above SEM results. In addition, the N_2 adsorption–desorption isotherm experiments results were displayed in Fig. S6 and Table S3. The pore size, pore volume, and specific surface area of HTCN have been measured to be 23.057 nm, 0.204 cm^3/g, and 32.982 m^2/g, which were about 1.2-times, 2.8-times, and 2.6-times than that of pure g-C_3N_4 (18.548 nm, 0.061 cm^3/g, and 10.625 m^2/g), respectively. In present study, the larger pore volume and enhanced specific surface area were caused by hollow porous tubular structure of HTCN, which could shorten the path of mass transfer and provide more reaction activity sites for improving the reaction probability and facilitating the photocatalytic performance of HTCN. According to Fig. 3d, a lot of S-CQDs were uniformly loaded on the surface of hollow tubular g-C_3N_4, and the lattice spacing of S-CQDs (0.21 nm) was determined by HRTEM. Fig. 3e and f reflected that the size of the pure S-CQDs was below 5 nm (average particle diameters were about 2 nm), the color of its solution was yellow, and its solution also showed homogeneous phase with no precipitations. What's more, the results of elemental mapping images (Fig. 3h–j) and the EDS of TEM (Fig. 3g) were acknowledged that HTCN-C(2) contained S, N and C species.

X-ray photoelectron spectroscopy (XPS) survey spectrum results (Fig. 4a) also presented that the HTCN-C(2) were mainly made up of oxygen, sulfur, nitrogen, and carbon. Among them, the peak of O element at 532.4 eV (Fig. S7) was belonging to the chemisorbed oxygen [49,50]. The high-resolution spectrum of C1s (Fig. 4b) showed two distinct peaks at 284.5 eV and 288.1 eV. The former peak around 284.5 eV was attributed to graphite sp^2 C—C, and the latter peak presents the presence of C=O [51]. As revealed in Fig. 4c, the N 1s peak was separated into four binding energy peaks at ~404.5 eV, 400.6 eV, 399.5 eV, and 398.8 eV, which could be assigned to the charging effects of π-excitations, pyrrolic type and pyridinic type N atoms (C—N=C, N—C_3, C—NH) [52]. In the analysis for S 2p (Fig. 4d), two significant peaks (165.1 eV and 163.8 eV) were observed. The lower peak (165.1 eV) was attributed to the C-S-C units, and the peak located at 163.8 eV was formed by replacing N atoms (C-S bonds) [53]. The analysis mentioned above performed that S-CQDs successfully decorated on the surface of HTCN with good dispersion.

3.2. Optical and electrochemical properties

The optical and electrochemical properties of resultant samples were characterized and depicted in Fig. 5. From Fig. 5a and the inset image of Fig. 5a, the S-CQDs/hollow tubular g-C_3N_4 hybrid

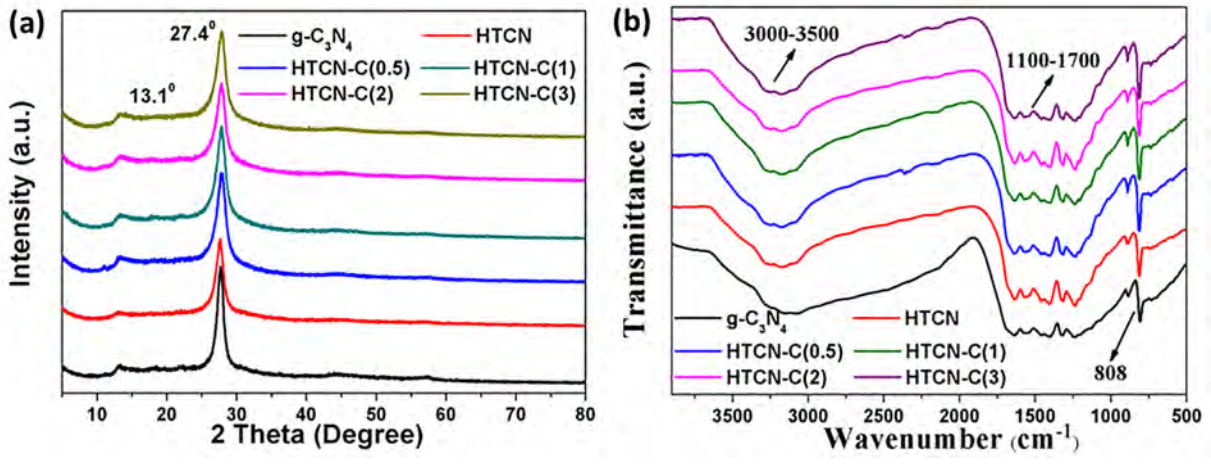

Fig. 1. XRD patterns (a); FT-IR spectra (b) of samples of bulk g-C_3N_4, HTCN, and HTCN-C(x), x = 0.5, 1, 2 and 3.

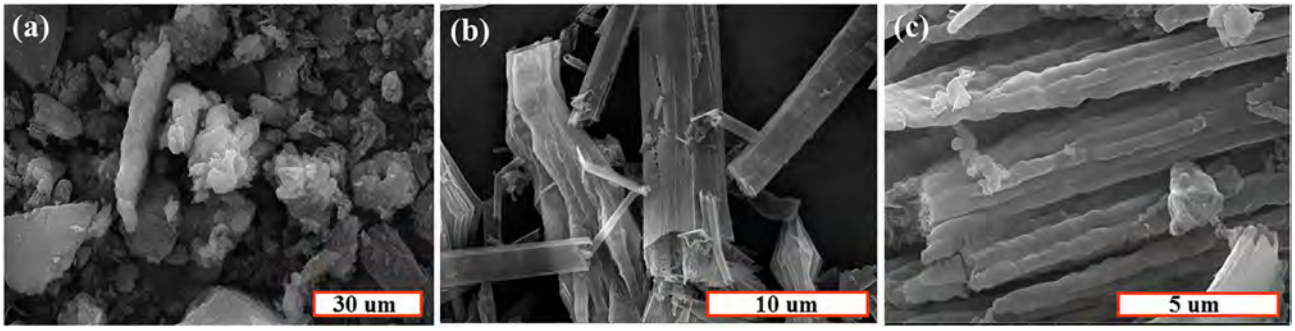

Fig. 2. SEM images of samples of (a) bulk g-C_3N_4, (b) HTCN, and (c) HTCN-C(2), respectively.

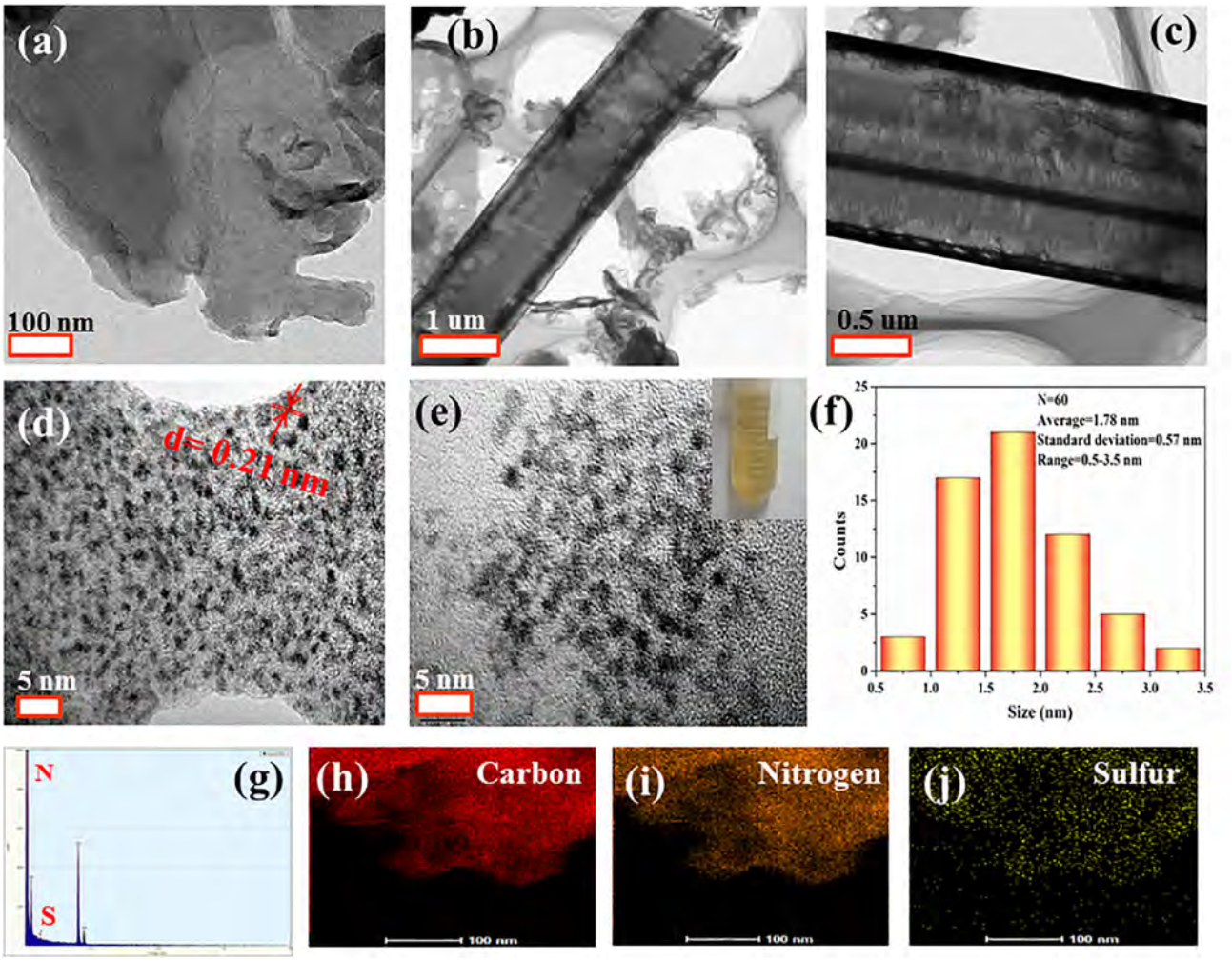

Fig. 3. TEM images of (a) bulk g-C_3N_4, (b) HTCN, (c, d) HTCN-C(2), and (e) pure S-CQDs, respectively. The inset in (e) is the digital photographs of pure S-CQDs solution. (f) Corresponding size distribution graph of (e) pure S-CQDs. The TEM EDS spectrum (g) and elemental mapping patterns (h, i, j) of HTCN-C(2).

photocatalyst (HTCN-C) extended the optical absorption regions of bulk g-C_3N_4 (about 470 nm). HTCN-C and HTCN presented a red shift in the absorption region compared to bulk g-C_3N_4 due to the excellent light harvest ability of S-CQDs and the porous structure of HTCN (Porous structure could promote the multiple reflection of incident light) [54,55]. Additionally, the band energy gap (Eg) of HTCN and HTCN-C(2) was calculated to be 2.53 eV and 2.47 eV via the Kubelk-Munk method (Fig. 5b). The HTCN-C(2) photocatalyst had a narrower bandgap than HTCN, leading to more light generated electrons under visible light irradiation. The value of valence band (VB) could obtained from VB XPS spectra [46,56]. As shown in Fig. 5c and d, the VB potential of HTCN and HTCN-C(2) was estimated to be 1.62 eV and 1.53 eV, respectively. Hence, the conduction band (CB) value of HTCN and HTCN-C(2) was calculated to be −0.91 eV and −0.94 eV by the formula of $E_{CB} = E_{VB} - Eg$. Where E_{VB}, Eg and E_{CB} were VB potential, the band gap energy and CB potential, respectively. The detailed location of VB and CB band of HTCN-C(2) was illustrated in Scheme 2.

To better expound the mechanism of electron delivery, PL technique and the time-resolved fluorescence spectra were conducted. Typically, 5 mg of sample was scattered in 4 mL of distilled water, and the above solution was sonicated for 240 min to obtain the suspension. And the suspension exhibited maximal emission peak at about 465 nm with

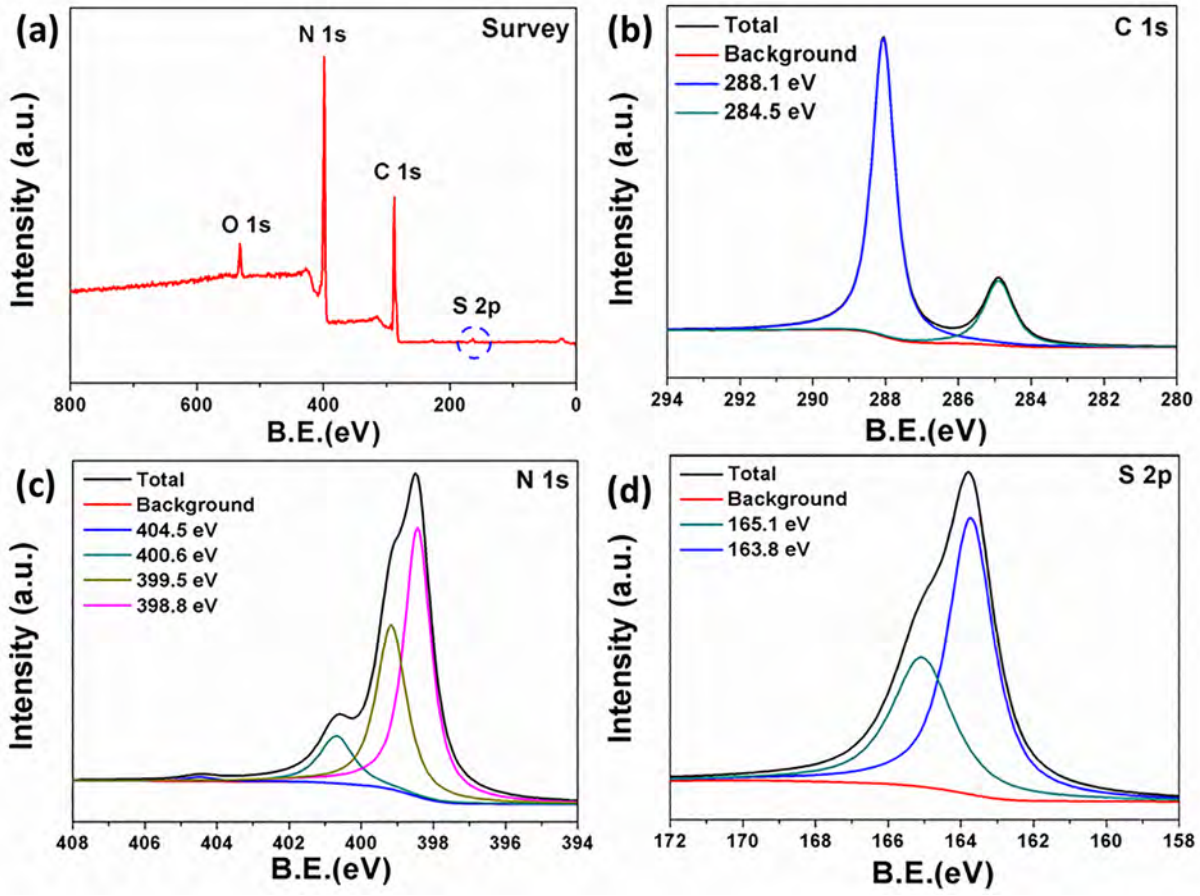

Fig. 4. High-resolution XPS spectra of (a) survey, (b) C 1s, (c) N 1s and (d) S 2p for HTCN-C(2).

340 nm excitation wavelength at room temperature measured by Fluromax-4 spectrofluorometer. From Fig. 5e, the sample of HTCN-C(2) exhibited the lowest PL intensity, indicating the excellent carriers separation, which was mainly caused by the hollow porous tubular structure of HTCN and the existence of S-CQDs [56,57]. Furthermore, non-modified g-C_3N_4 exhibited the highest PL intensity in all prepared photocatalysts, demonstrating that the modified g-C_3N_4 could improve the photocatalytic activity by efficient reducing the recombination rate

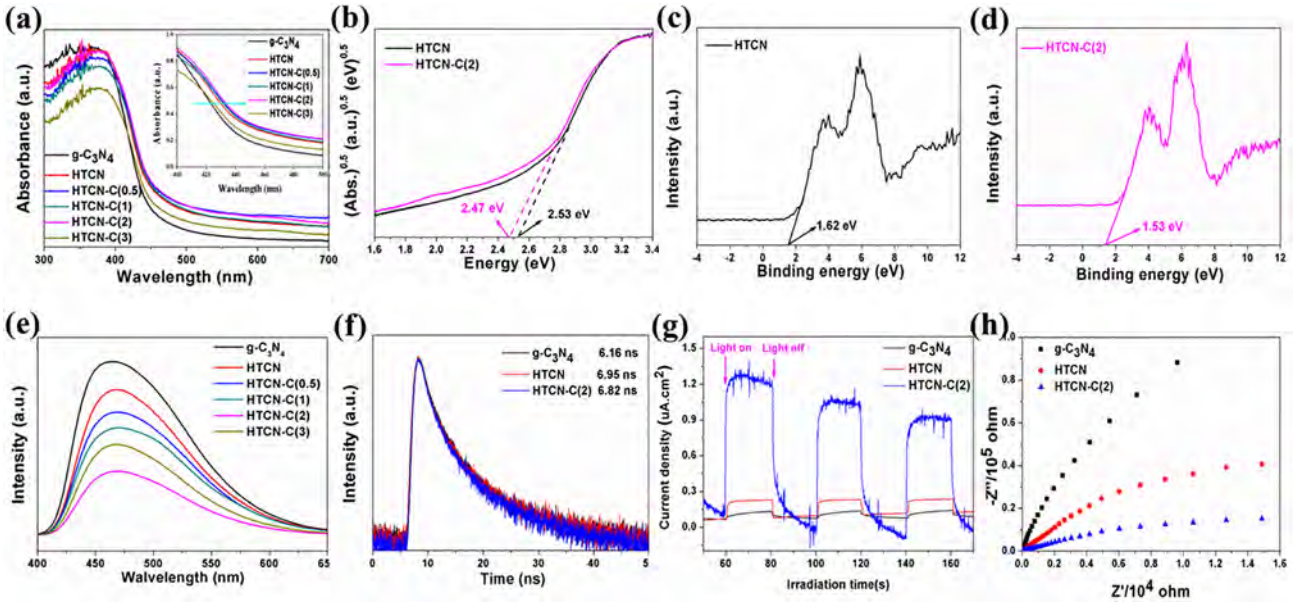

Fig. 5. (a) UV–vis diffuse reflectance spectra of samples and (b) band gap of HTCN and HTCN-C(2); XPS valence band spectra of (c) HTCN and (d) HTCN-C(2), respectively. (e) PL spectra of samples and (f) Time-resolved PL spectra, (g) Photocurrent responses under visible light, (h) EIS Nyquist plots for bulk g-C_3N_4, HTCN and HTCN-C(2) samples.

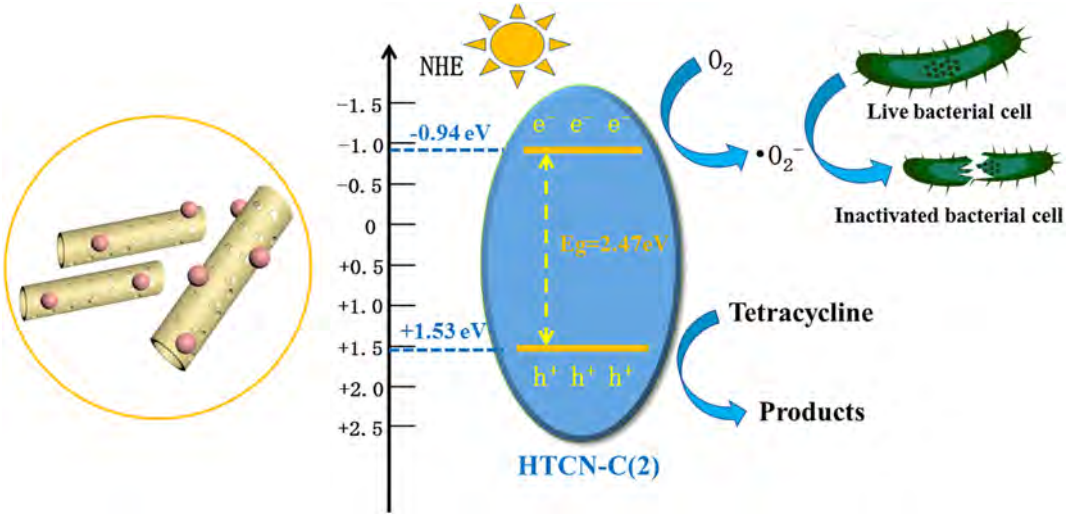

Scheme 2. Possible photocatalytic mechanism scheme of HTCN-C(2) composite for TC degradation and photocatalytic inactivation toward *Escherichia coli* under visible light irradiation.

of carriers. Moreover, the time-resolved fluorescence decay spectrum also verified above results and depicted in Fig. 5f. The fitting results were given in Table S4. The average life-time ($\tau_{average}$) was calculated by the Eq of $\tau_{average} = (A_1\tau_1^2 + A_2\tau_2^2)/(A_1\tau_1 + A_2\tau_2)$. The $\tau_{average}$ of bulk g-C_3N_4, HTCN, and HTCN-C(2) were 6.16, 6.95 and 6.82 ns, respectively. Consequently, the mean lifetimes of HTCN and HTCN-C(2) were longer than bulk g-C_3N_4, which was due to the improved specific surface area. The values showed an extended lifetime of light-generated carriers over HTCN and HTCN-C(2) samples, and hence promoting the process of interfacial charge migration [56]. Compared to HTCN, HTCN-C(2) displayed a shorten lifetime of electron/hole pairs, which could be ascribed to the presence of non-radiative quenching routes [58].

The transient photocurrent responses and electrochemical impedance spectroscopy were crucial factors to evaluate the separation and transfer efficiency of carriers. As displayed in Fig. 5g, HTCN exhibited a larger photocurrent intensity than bulk g-C_3N_4, and HTCN-C(2) showed the highest photocurrent signs indicating the best e^-/h^+ separation efficiency. It was easy to found that photocurrent intensity of HTCN-C(2) was approximately a 17.5-fold and 6.56-fold increase compared to bulk g-C_3N_4 and HTCN, respectively. Additionally, the transient photocurrent values of photocatalysts almost maintained repeatedly after several ON/OFF illumination cycles, indicating the good photoelectrochemical stability. The radius of arc was always connected with the charge transfer resistance at the electrode-electrolyte interface, and the EIS spectra of corresponding samples were shown in Fig. 5h. From Fig. 5h, the size of the arc radius order was HTCN-C(2) < HTCN < bulk g-C_3N_4, and HTCN-C(2) presents a lowest charge

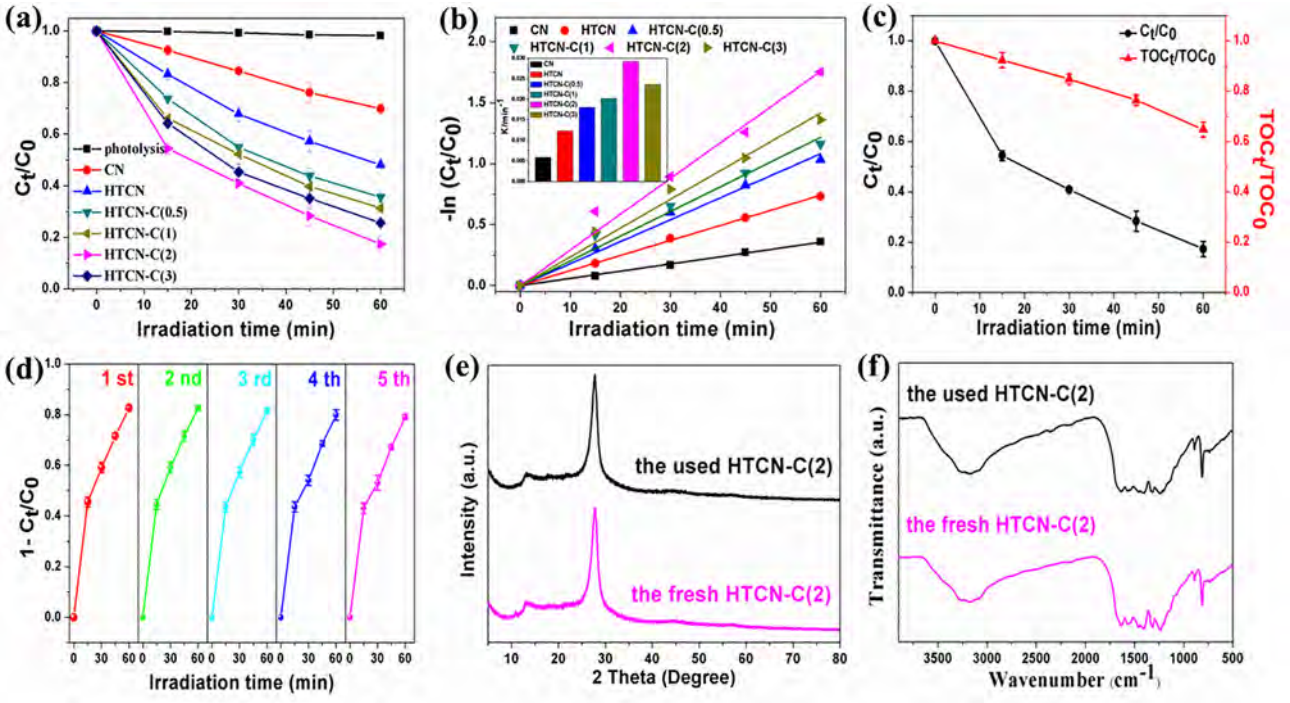

Fig. 6. (a) Photocatalytic degradation of TC over as-obtained samples; (b) Pseudo first-order kinetic fitting curves and the corresponding apparent rate constants (K_{app}); (c) The photocatalytic degradation and TOC removal curves of TC on HTCN-C(2) catalyst; (d) The cycling test for the degradation of TC by the fresh and used HTCN-C(2) catalyst; (e) XRD and (f) FT–IR survey for fresh and used HTCN-C(2) sample.

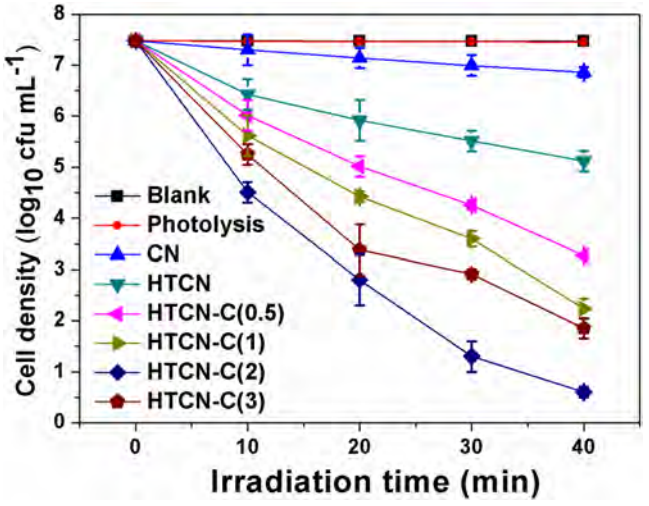

Fig. 7. Inactivation efficiencies of as-prepared samples toward *E. coli* (3.0×10^7 CFU/mL) under visible light irradiation.

transfer resistance and best interfacial charge migration skill. These results were well fitted with PL and TRPL analysis, indicating hollow porous tubular structure of HTCN and loading of S-CQDs have synergistic effect to enhance the photocatalytic performance.

3.3. Photocatalytic activities and mechanisms

3.3.1. Photocatalytic degradation of TC

As a typical antibiotic, TC has been extensively applied in agriculture, animal husbandry and iatrology. Previous researches illuminated that TC was a stable pharmaceutical and poorly metabolized in animals, and couldn't be degraded under light irradiation without photocatalysts [59,60]. In this work, the photocatalytic properties of resultant composites were studied via the removal of TC in aqueous solution under visible light irradiation (Fig. 6a). Before visible light irradiation, the adsorption-desorption equilibrium was attained between TC and the samples under the condition of 1 h dark reaction [61]. As shown in Fig. S8, the adsorption efficiency of TC for bulk g-C_3N_4, HTCN and HTCN-C(2) was only 2.98%, 3.88% and 5.37%, respectively. For Fig. 6a, different samples exhibited different photodegradation properties, which was in order of bulk g-C_3N_4 (30.16%) < HTCN (51.85%) < HTCN-C(0.5) (64.41%) < HTCN-C(1) (68.66%) < HTCN-C(3) (74.40%) < HTCN-C(2) (82.67%). Obviously, the removal capacity of HTCN-C photocatalysts were all better than bulk g-C_3N_4 and HTCN, indicating the presence of S-CQDs facilitated the photocatalytic degradation efficiency of HTCN. However, the photocatalytic activity of HTCN-C did not increase as the proportion of S-CQDs increased. It could be attributed to the fact that proper amount of S-CQDs could act as an electron mediator to accelerate separation of carriers, whereas excessive S-CQDs would compete for photons with g-C_3N_4 and led to a lower reactive species (inner filter effects) [62]. The experimental results were deep studied via the pseudo-first-order kinetic model with an Eq of ln (C_t/C_0) = -K_{app}t. From the kinetic curves (Fig. 6b) and apparent rate constant (inset in Fig. 6b), the HTCN-C(2) possessed the highest K_{app} (0.0293 min^{-1}), which was ~2.36-fold bigger than HTCN (0.0124 min^{-1}) and ~4.97-fold bigger than that of bulk g-C_3N_4 (0.0059 min^{-1}). Hence, the above-mentioned results were in line with the before properties characterization analysis, confirming the sample of HTCN-C(2) has optimum photocatalytic activity.

In order to deeper evaluate the property of the photocatalyst of HTCN-C(2), total organic carbon (TOC) removal analysis and multiple cycles experimental were also investigated and the corresponding curves were described in Fig. 6c and d. From Fig. 6c, the mineralization efficiency of HTCN-C(2) could achieved 35.22% within 60 min visible light irradiation. Under the same reaction conditions, the used HTCN-C(2) was washed and collected for cycles experimental (Fig. 6d). After five repeated cycles, the photo-degradation efficiency of HTCN-C(2) showed negligible decrease (about 3.52% lost) and remained about 79.15% efficiency. The aforementioned results exhibited the sample of HTCN-C(2) has the ability to degrade TC into intermediate products or CO_2, and showed good chemical stability and reusability, which benefited the practical application. Furthermore, the recycled HTCN-C(2) was measured by XRD and FT-IR (Fig. 6e and f). It was acknowledged that the recycled HTCN-C(2) kept its intrinsically crystal structure, exhibiting no apparent difference between fresh and recycled HTCN-C(2). In addition, as illustrated in Table S2, the S/C ratio of recycled HTCN-C(2) was similar to that of fresh HTCN-C(2). In a word, the sample of HTCN-C(2) was an capable and recyclable photocatalyst, which shows great application potential for practical water application.

3.3.2. Photocatalytic disinfection performance

E. coli inactivation was chosen for probing the disinfection ability of resultant samples, and corresponding results were depicted in Fig. 7. It could be observed that the influence of visible light on bacteria was insignificant, because the density of viable *E. coli* cells kept almost unchanged with light control and no photocatalysts. Furthermore, blank reaction (catalysts without light irradiation) was to prove that the material itself was also not toxic to bacteria under the condition of dark. But the amount of viable *E. coli* cells began to decrease after the addition of the samples in the visible light. From Fig. 7, only about 0.62-log and 2.36-log reduction of *E. coli* cells by bulk g-C_3N_4 and HTCN were achieved under 40 min of visible light irradiation. In contrast, HTCN-C nanocomposites showed more excellent disinfection performance and about 4.21-log, 5.24-log, 6.88-log, and 5.63-log reduction of *E. coli* cells for HTCN-C(0.5), HTCN-C(1), HTCN-C(2), and HTCN-C(3), respectively. Apparently, HTCN-C(2) displays the highest inactivation efficiencies and meet the requirement of surface water treatment.

In the process of studying the mechanism of photocatalytic

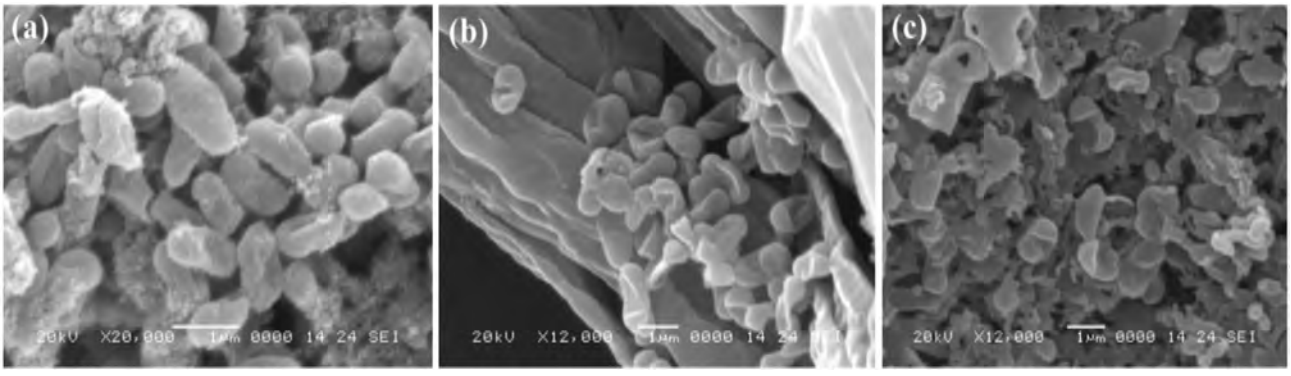

Fig. 8. SEM images of *E. coli* treated by HTCN-C(2) hybrid photocatalysts under visible light irradiation at 0 min, 20 min, and 40 min.

disinfection, bacterial regrowth experiment was an important index [63–66]. Hence, the damage of the cell membrane and the morphological structure destructs of *E. coli* were investigated by SEM, and the corresponding preparation procedures for bacterial SEM study were put in the supporting information. Prior to photocatalytic disinfection process, *E. coli* cells possessed a normal rod-like morphology as well as regular fuzzy elliptical outlines (Fig. 8a). In contrast, the typical rod shape of the *E. coli* cell was destructed with holes and showed an abnormal morphology after 30 min or 60 min visible light irradiation (Fig. 8b and c). This phenomenon shown that the cell membrane was damaged during the inactivation process, which subsequently leads to severe leakage of intracellular components. The leakage of potassium ion (K^+) could acted as an index to evaluate cell membrane permeability and evaluated membrane destruction, because K^+ was virtually existing in bacteria. As shown in Fig. S9, there was little K^+ leakage found in the light control, indicating a few cell death and structure destruction. However, quick leakage of K^+ occurred in HTCN-C(2) photocatalytic disinfection system, suggesting that the cell was inactivated and the active species (h^+, $^{\cdot}O2^-$ and H_2O_2) were generated under the visible light irradiation [67–70].

3.3.3. Possible reaction mechanism

For better understanding the possible photocatalytic reaction mechanisms about antibiotic degradation and bacterial inactivation, the roles of major active substances were systemically researched. And the corresponding scavengers were TEMPOL, EDTA-2Na, and TBA, which could assimilate reactive species of $^{\cdot}O2^-$, h^+, and $^{\cdot}OH$, respectively [71]. From Fig. 9a, there was a significant photocatalytic activity deterioration with the addition of TEMPOL (5 mM) and EDTA-2Na (5 mM), presenting the predominant roles of $^{\cdot}O2^-$ and h^+ in the photocatalytic reaction process. Moreover, slight inhibition (about 6.78% loss after 1 h) can be found with the addition of TBA (5 mM), which indicated that $^{\cdot}OH$ also participates in the degradation of TC. The relevant values of TC removal ratio with the presence of scavengers were shown in the inset of Fig. 9a. Hence, the main active species for HTCN-C(2) might be $^{\cdot}O2^-$ and h^+. Some similar results were discovered in the process of bacterial inactivation with the existence of various quenchers (Fig. 9b). As described in Fig. 9b, $^{\cdot}O2^-$ and h^+ still play an vital role in controlling the process of inactivation, and ·OH acts as an assistant. Thus, $^{\cdot}O2^-$ and h^+ affect the process of photocatalytic inactivation and the removal of TC, and the function of $^{\cdot}OH$ could not be ignored either. In order to further affirmed that $^{\cdot}O2^-$ and $^{\cdot}OH$ were yielded in the HTCN-C(2) photocatalytic system, and the ESR spin-trap measurement was conducted under visible light irradiation. From Fig. 9c and d, there was no signal peaks of DMPO-$^{\cdot}O2^-$ and DMPO-$^{\cdot}OH$ appeared in the darkness, while obvious intensity signals can be detected under visible light. Therefore, $^{\cdot}O2^-$, h^+, and $^{\cdot}OH$ active species were generated and had synergistic effect during the photocatalytic process based on the ESR analysis and the trapping experiments.

Based on the aforementioned analyses and discussions, a deep mechanism for TC degradation and photocatalytic inactivation toward *Escherichia coli* over HTCN-C(2) composite under visible light irradiation was presented in Scheme 2. In this system, S-CQDs were acted as a photosensitizer and an electron mediator to broaden photon absorption region and decrease photo-induced e^-/h^+ recombination. The electrons (e^-) of HTCN-C(2) composite were excited from VB to CB, and

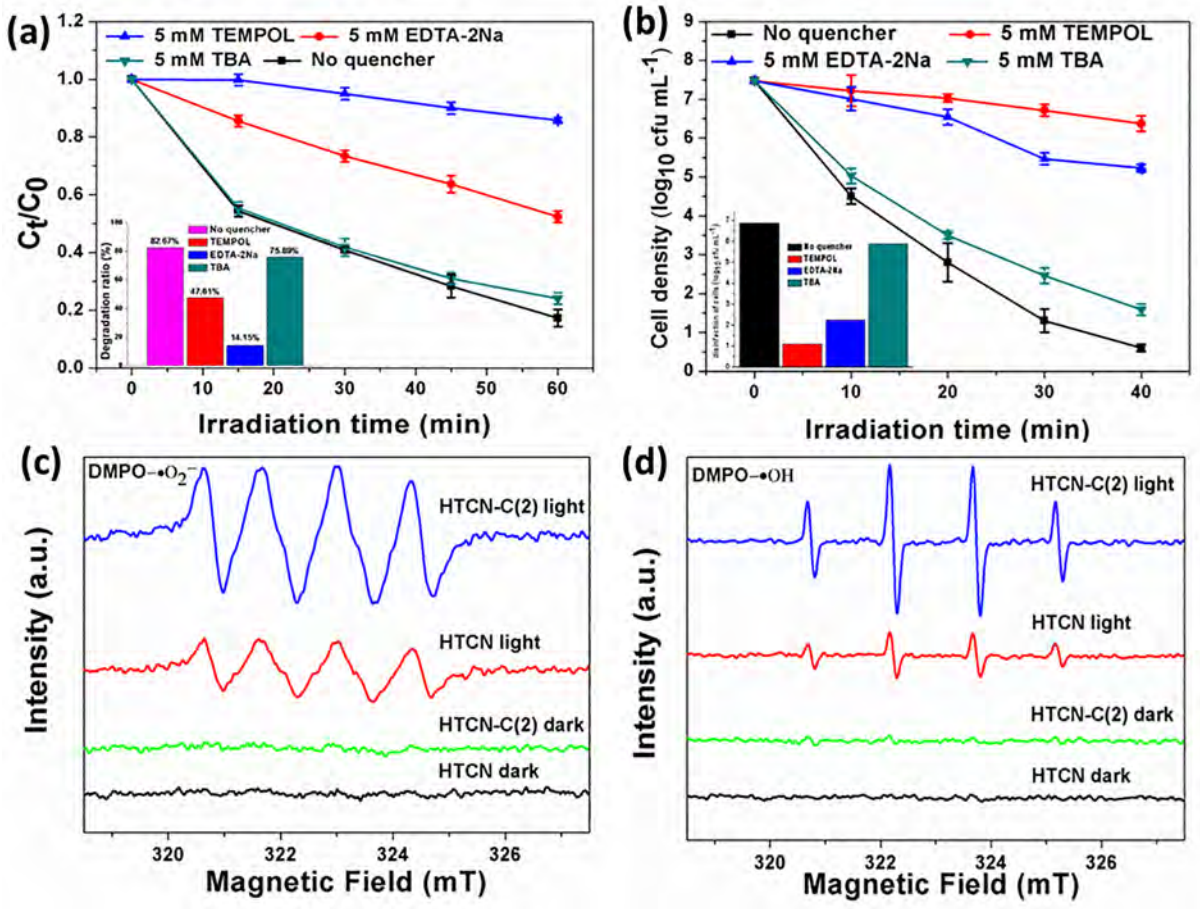

Fig. 9. (a) Photocatalytic activities of the HTCN-C(2) sample for the degradation of TC under the condition of different quenchers; (b) Inactivation efficiency of the HTCN-C(2) sample toward *E. coli* under the condition of different quenchers; ESR spectra of radical adducts tapped by DMPO spin-trapping in HTCN-C(2) dispersion in the dark and under visible light irradiation (c) in methanol dispersion for DMPO − $^{\cdot}O_2^-$ and (d) in aqueous dispersion for DMPO − $^{\cdot}OH$.

generated holes (h^+) in the VB under visible light. The accumulated e^- can validly capture O_2 to obtain $^{\cdot}O_2^-$, and $^{\cdot}O_2^-$ could reacted with H^+ to form H_2O_2. The obtained $^{\cdot}OH$ of HTCN-C(2) may come from the conversion of the H_2O_2. In addition, the h^+ of HTCN-C(2) also made contribution to reacting with TC and photocatalytic inactivation toward *Escherichia coli*. In brief, reactive radicals such as h^+, $^{\cdot}O_2^-$ and $^{\cdot}OH$ can participate in the process of photocatalytic inactivation and photo-degradation, which was consistent with ESR analysis and the trapping experiments. Hence, HTCN-C(2) displayed an excellent inactivation efficiency and superior photocatalytic degradation activity, which meet the requirement of surface water treatment.

4. Conclusion

In summary, we have successfully fabricated modified CQDs loaded hollow tubular g-C_3N_4 novel photocatalyst (HTCN-C) via ultrasonic-assisted method. The hollow tubular g-C_3N_4 was prepared via a molecule self-assembly between melamine and cyanuric acid. Based on the characterization of morphologies and optical properties, the HTCN-C hybrid system was formed with modified CQDs loaded on the surface of hollow tubular g-C_3N_4. In this photocatalytic system, S-CQDs were acted as a photosensitizer and an electron mediator to broaden photon absorption region and decrease photo-induced carrier recombination. Compared to bulk g-C_3N_4, the optimal photocatalyst (HTCN-C(2)) displayed superior photocatalytic activity for TC degradation and photocatalytic inactivation toward *Escherichia coli*, with the 82.67% removal rate of tetracycline and the inactivation of 6.88 $\log_{10}$ cfu mL^{-1} (about 99.99% destruction rate) of bacterial cells under visible-light irradiation, respectively. Eventually, possible reaction mechanism for enhancing the photocatalytic activity of antibiotic degradation and bacterial inactivation was raised. These results offered a novel clue for the design of 0D/1D g-C_3N_4-based photocatalyst with advanced nanostructure for practical wastewater treatment.

Acknowledgements

The authors would like to thank Hai Guo for his assistance with the PL measurements, Wanyue Dong for her assistance with the DRS measurements and Danling Guan for her assistance in destruction of *Escherichia coli*. This study was financially supported by the Program for the National Natural Science Foundation of China (81773333, 51879101, 51809090, 51579098, 51779090, 51709101, 51709100, 51278176, 51521006, 51378190, 51408206), the National Program for Support of Top-Notch Young Professionals of China (2014), the Fundamental Research Funds for the Central Universities, Hunan Provincial Science and Technology Plan Project (No. 2016RS3026, 2017SK2243, 2018SK20410), the Program for New Century Excellent Talents in University (NCET-13-0186), the Fundamental Research Funds for the Central Universities (531107051080, 531109200027, 531107050978), Hunan Provincial Innovation Foundation For Postgraduate (CX2018B195), and the Program for Changjiang Scholars and Innovative Research Team in University (IRT-13R17).

Appendix A. Supplementary data

Supplementary data to this article can be found online at https://doi.org/10.1016/j.cej.2019.122132.

References

[1] H. Wang, Z. Zeng, P. Xu, L. Li, G. Zeng, R. Xiao, Z. Tang, D. Huang, L. Tang, C. Lai, D. Jiang, Y. Liu, H. Yi, L. Qin, S. Ye, X. Ren, W. Tang, Recent progress in covalent organic framework thin films: fabrications, applications and perspectives, Chem. Soc. Rev. 48 (2018) 488–516.

[2] C. Zhang, W. Wang, A. Duan, G. Zeng, D. Huang, C. Lai, X. Tan, M. Cheng, R. Wang, C. Zhou, W. Xiong, Y. Yang, Adsorption behavior of engineered carbons and carbon nanomaterials for metal endocrine disruptors: experiments and theoretical calculation, Chemosphere 222 (2019) 184–194.

[3] W. Wang, M. Chen, D. Huang, G. Zeng, C. Zhang, C. Lai, C. Zhou, Y. Yang, M. Cheng, L. Hu, W. Xiong, Z. Li, Z. Wang, An overview on nitride and nitrogen-doped photocatalysts for energy and environmental applications, Compos. Part B: Eng. 172 (2019) 704–723.

[4] L. Qin, D. Huang, P. Xu, G. Zeng, C. Lai, Y. Fu, H. Yi, B. Li, C. Zhang, M. Cheng, C. Zhou, X. Wen, In-situ deposition of gold nanoparticles onto polydopamine-decorated g-C_3N_4 for highly efficient reduction of nitroaromatics in environmental water purification, J. Colloid Interface Sci. 534 (2019) 357–369.

[5] S. Chen, D. Huang, G. Zeng, X. Gong, W. Xue, J. Li, Y. Yang, C. Zhou, Z. Li, X. Yan, T. Li, Q. Zhang, Modifying delafossite silver ferrite with polyaniline: visible-light-response Z-scheme heterojunction with charge transfer driven by internal electric field, Chem. Eng. J. 370 (2019) 1087–1100.

[6] P. Xu, G.M. Zeng, D.L. Huang, C.L. Feng, S. Hu, M.H. Zhao, C. Lai, Z. Wei, C. Huang, G.X. Xie, Z.F. Liu, Use of iron oxide nanomaterials in wastewater treatment: a review, Sci. Total Environ. 424 (2012) 1–10.

[7] Y. Yang, C. Zhang, C. Lai, G. Zeng, D. Huang, M. Cheng, J. Wang, F. Chen, C. Zhou, W. Xiong, BiOX (X = Cl, Br, I) photocatalytic nanomaterials: applications for fuels and environmental management, Adv. Colloid Interface Sci. 254 (2018) 76–93.

[8] S. Ye, G. Zeng, H. Wu, C. Zhang, J. Liang, J. Dai, Z. Liu, W. Xiong, J. Wan, P. Xu, M. Cheng, Co-occurrence and interactions of pollutants, and their impacts on soil remediation—a review, Crit. Rev. Environ. Sci. Technol. 47 (2017) 1528–1553.

[9] S. Ye, M. Yan, X. Tan, J. Liang, G. Zeng, H. Wu, B. Song, C. Zhou, Y. Yang, H. Wang, Facile assembled biochar-based nanocomposite with improved graphitization for efficient photocatalytic activity driven by visible light, Appl. Catal. B: Environ. 250 (2019) 78–88.

[10] H. Yi, M. Yan, D. Huang, G. Zeng, C. Lai, M. Li, X. Huo, L. Qin, S. Liu, X. Liu, B. Li, H. Wang, M. Shen, Y. Fu, X. Guo, Synergistic effect of artificial enzyme and 2D nano-structured Bi_2WO_6 for eco-friendly and efficient biomimetic photocatalysis, Appl. Catal. B: Environ. 250 (2019) 52–62.

[11] H. Guo, C.-G. Niu, D.-W. Huang, N. Tang, C. Liang, L. Zhang, X.-J. Wen, Y. Yang, W.-J. Wang, G.-M. Zeng, Integrating the plasmonic effect and p-n heterojunction into a novel Ag/Ag_2O/$PbBiO_2Br$ photocatalyst: broadened light absorption and accelerated charge separation co-mediated highly efficient visible/NIR light photocatalysis, Chem. Eng. J. 360 (2019) 349–363.

[12] H. Guo, H.-Y. Niu, C. Liang, C.-G. Niu, D.-W. Huang, L. Zhang, N. Tang, Y. Yang, C.-Y. Feng, G.-M. Zeng, Insight into the energy band alignment of magnetically separable Ag_2O/$ZnFe_2O_4$ p-n heterostructure with rapid charge transfer assisted visible light photocatalysis, J. Catal. 370 (2019) 289–303.

[13] W. Xiong, G. Zeng, Z. Yang, Y. Zhou, C. Zhang, M. Cheng, Y. Liu, L. Hu, J. Wan, C. Zhou, Adsorption of tetracycline antibiotics from aqueous solutions on nanocomposite multi-walled carbon nanotube functionalized MIL-53 (Fe) as new adsorbent, Sci. Total Environ. 627 (2018) 235–244.

[14] C. Zhang, L. Liu, G.-M. Zeng, D.-L. Huang, C. Lai, C. Huang, Z. Wei, N.-J. Li, P. Xu, M. Cheng, Utilization of nano-gold tracing technique: study the adsorption and transmission of laccase in mediator-involved enzymatic degradation of lignin during solid-state fermentation, BioChem. Eng. J. 91 (2014) 149–156.

[15] C. Zhang, C. Lai, G. Zeng, D. Huang, L. Tang, C. Yang, Y. Zhou, L. Qin, M. Cheng, Nanoporous Au-based chronocoulometric aptasensor for amplified detection of Pb^{2+} using DNAzyme modified with Au nanoparticles, Biosens. Bioelectron. 81 (2016) 61–67.

[16] C. Zhang, G. Zeng, D. Huang, C. Lai, M. Chen, M. Cheng, W. Tang, L. Tang, H. Dong, B. Huang, X. Tan, R. Wang, Biochar for environmental management: mitigating greenhouse gas emissions, contaminant treatment, and potential negative impacts, Chem. Eng. J. 373 (2019) 902–922.

[17] C. Zhang, C. Lai, G. Zeng, D. Huang, C. Yang, Y. Wang, Y. Zhou, M. Cheng, Efficacy of carbonaceous nanocomposites for sorbing ionizable antibiotic sulfamethazine from aqueous solution, Water Res. 95 (2016) 103–112.

[18] G. Zeng, C. Zhang, D. Huang, C. Lai, L. Tang, Y. Zhou, P. Xu, H. Wang, L. Qin, M. Cheng, Practical and regenerable electrochemical aptasensor based on nanoporous gold and thymine-Hg^{2+}-thymine base pairs for Hg^{2+} detection, Biosens. Bioelectron. 90 (2017) 542–548.

[19] M. Cheng, G. Zeng, D. Huang, C. Lai, Y. Liu, C. Zhang, R. Wang, L. Qin, W. Xue, B. Song, S. Ye, H. Yi, High adsorption of methylene blue by salicylic acid–methanol modified steel converter slag and evaluation of its mechanism, J. Colloid. Interface Sci. 515 (2018) 232–239.

[20] K. He, G. Chen, G. Zeng, A. Chen, Z. Huang, J. Shi, T. Huang, M. Peng, L. Hu, Three-dimensional graphene supported catalysts for organic dyes degradation, Appl. Catal. B: Environ. 228 (2018) 19–28.

[21] Y. Wang, Y. Zhu, Y. Hu, G. Zeng, Y. Zhang, C. Zhang, C. Feng, How to construct DNA hydrogels for environmental applications: advanced water treatment and environmental analysis, Small 14 (2018) e1703305.

[22] Q. He, P. Xu, C. Zhang, G. Zeng, Z. Liu, D. Wang, W. Tang, H. Dong, X. Tan, A. Duan, Influence of surfactants on anaerobic digestion of waste activated sludge: acid and methane production and pollution removal, Crit. Rev. Biotechnol. 39 (2019) 746–757.

[23] W. Xue, D. Huang, J. Li, G. Zeng, R. Deng, Y. Yang, S. Chen, Z. Li, X. Gong, B. Li, Assembly of AgI nanoparticles and ultrathin g-C_3N_4 nanosheets codecorated Bi_2WO_6 direct dual Z-scheme photocatalyst: an efficient, sustainable and heterogeneous catalyst with enhanced photocatalytic performance, Chem. Eng. J. 373 (2019) 1144–1157.

[24] L. Qin, G. Zeng, C. Lai, D. Huang, C. Zhang, P. Xu, T. Hu, X. Liu, M. Cheng, Y. Liu, L. Hu, Y. Zhou, A visual application of gold nanoparticles: simple, reliable and sensitive detection of kanamycin based on hydrogen-bonding recognition, Sens. Actuat. B 243 (2017) 946–954.

[25] B. Song, P. Xu, G. Zeng, J. Gong, P. Zhang, H. Feng, Y. Liu, X. Ren, Carbon

nanotube-based environmental technologies: the adopted properties, primary mechanisms, and challenges, Rev. Environ. Sci. Biol. 17 (2018) 571–590.
[26] C. Zhou, C. Lai, C. Zhang, G. Zeng, D. Huang, M. Cheng, L. Hu, W. Xiong, M. Chen, J. Wang, Y. Yang, L. Jiang, Semiconductor/boron nitride composites: synthesis, properties, and photocatalysis applications, Appl. Catal. B: Environ. 238 (2018) 6–18.
[27] W. Xiong, Z. Zeng, G. Zeng, Z. Yang, R. Xiao, X. Li, J. Cao, C. Zhou, H. Chen, M. Jia, Y. Yang, W. Wang, X. Tang, Metal-organic frameworks derived magnetic carbon-αFe/Fe_3C composites as a highly effective adsorbent for tetracycline removal from aqueous solution, Chem. Eng. J. 374 (2019) 91–99.
[28] K. Wang, Y. Li, G. Zhang, J. Li, X. Wu, 0D Bi nanodots/2D Bi_3NbO_7 nanosheets heterojunctions for efficient visible light photocatalytic degradation of antibiotics: enhanced molecular oxygen activation and mechanism insight, Appl. Catal. B: Environ. 240 (2019) 39–49.
[29] Y. Lin, S. Wu, C. Yang, M. Chen, X. Li, Preparation of size-controlled silver phosphate catalysts and their enhanced photocatalysis performance via synergetic effect with MWCNTs and PANI, Appl. Catal. B: Environ. 245 (2019) 71–86.
[30] T. Guo, K. Wang, G. Zhang, X. Wu, A novel α-Fe_2O_3@g-C_3N_4 catalyst: synthesis derived from Fe-based MOF and its superior photo-Fenton performance, Appl. Surf. Sci. 469 (2019) 331–339.
[31] C. Liu, H. Huang, W. Cui, F. Dong, Y. Zhang, Band structure engineering and efficient charge transport in oxygen substituted g-C_3N_4 for superior photocatalytic hydrogen evolution, Appl. Catal. B: Environ. 230 (2018) 115–124.
[32] Q. Liang, Z. Li, X. Yu, Z.H. Huang, F. Kang, Q.H. Yang, Macroscopic 3D porous graphitic carbon nitride monolith for enhanced photocatalytic hydrogen evolution, Adv. Mater. 27 (2015) 4634–4639.
[33] C. Liu, H. Huang, L. Ye, S. Yu, N. Tian, X. Du, T. Zhang, Y. Zhang, Intermediate-mediated strategy to horn-like hollow mesoporous ultrathin g-C_3N_4 tube with spatial anisotropic charge separation for superior photocatalytic H_2 evolution, Nano Energy 41 (2017) 738–748.
[34] X. Chen, Q. Liu, Q. Wu, P. Du, J. Zhu, S. Dai, S. Yang, Incorporating graphitic carbon nitride (g-C_3N_4) quantum dots into bulk-heterojunction polymer solar cells leads to efficiency enhancement, Adv. Funct. Mater. 26 (2016) 1719–1728.
[35] L. Zhang, N. Ding, L. Lou, K. Iwasaki, H. Wu, Y. Luo, D. Li, K. Nakata, A. Fujishima, Q. Meng, localized surface plasmon resonance enhanced photocatalytic hydrogen evolution via Pt@Au NRs/C_3N_4 nanotubes under visible-light irradiation, Adv. Funct. Mater. 29 (2019) 1806774.
[36] C. Zhou, R. Shi, L. Shang, L.-Z. Wu, C.-H. Tung, T. Zhang, Template-free large-scale synthesis of g-C_3N_4 microtubes for enhanced visible light-driven photocatalytic H2 production, Nano Res. 11 (2018) 3462–3468.
[37] S. Fang, Y. Xia, K. Lv, Q. Li, J. Sun, M. Li, Effect of carbon-dots modification on the structure and photocatalytic activity of g-C_3N_4, Appl. Catal. B: Environ. 185 (2016) 225–232.
[38] J. Wang, L. Tang, G. Zeng, Y. Deng, H. Dong, Y. Liu, L. Wang, B. Peng, C. Zhang, F. Chen, 0D/2D interface engineering of carbon quantum dots modified Bi_2WO_6 ultrathin nanosheets with enhanced photoactivity for full spectrum light utilization and mechanism insight, Appl. Catal. B: Environ. 222 (2018) 115–123.
[39] M. Li, M. Wang, L. Zhu, Y. Li, Z. Yan, Z. Shen, X. Cao, Facile microwave assisted synthesis of N-rich carbon quantum dots/dual-phase TiO_2 heterostructured nanocomposites with high activity in CO_2 photoreduction, Appl. Catal. B: Environ. 231 (2018) 269–276.
[40] J. Zhang, M. Yan, X. Yuan, M. Si, L. Jiang, Z. Wu, H. Wang, G. Zeng, Nitrogen doped carbon quantum dots mediated silver phosphate/bismuth vanadate Z-scheme photocatalyst for enhanced antibiotic degradation, J. Colloid Interface Sci. 529 (2018) 11–22.
[41] J. Li, K. Liu, J. Xue, G. Xue, X. Sheng, H. Wang, P. Huo, Y. Yan, CQDS preluded carbon-incorporated 3D burger-like hybrid ZnO enhanced visible-light-driven photocatalytic activity and mechanism implication, J. Catal. 369 (2019) 450–461.
[42] Y. Dong, H. Pang, H.B. Yang, C. Guo, J. Shao, Y. Chi, C.M. Li, T. Yu, Carbon-based dots co-doped with nitrogen and sulfur for high quantum yield and excitation-independent emission, Angewandte Chemie 52 (2013) 7800–7804.
[43] Q. Xu, P. Pu, J. Zhao, C. Dong, C. Gao, Y. Chen, J. Chen, Y. Liu, H. Zhou, Preparation of highly photoluminescent sulfur-doped carbon dots for Fe(iii) detection, J. Mater. Chem. A 3 (2015) 542–546.
[44] W. Wang, P. Xu, M. Chen, G. Zeng, C. Zhang, C. Zhou, Y. Yang, D. Huang, C. Lai, M. Cheng, L. Hu, W. Xiong, H. Guo, M. Zhou, Alkali metal-assisted synthesis of graphite carbon nitride with tunable band-gap for enhanced visible-light-driven photocatalytic performance, ACS Sustain. Chem. Eng. 6 (2018) 15503–15516.
[45] C. Zhou, P. Xu, C. Lai, C. Zhang, G. Zeng, D. Huang, M. Cheng, L. Hu, W. Xiong, X. Wen, L. Qin, J. Yuan, W. Wang, Rational design of graphic carbon nitride copolymers by molecular doping for visible-light-driven degradation of aqueous sulfamethazine and hydrogen evolution, Chem. Eng. J. 359 (2019) 186–196.
[46] Y. Yang, C. Zhang, D. Huang, G. Zeng, J. Huang, C. Lai, C. Zhou, W. Wang, H. Guo, W. Xue, R. Deng, M. Cheng, W. Xiong, Boron nitride quantum dots decorated ultrathin porous g-C_3N_4: intensified exciton dissociation and charge transfer for promoting visible-light-driven molecular oxygen activation, Appl. Catal. B: Environ. 245 (2019) 87–99.
[47] W. Liu, Y. Li, F. Liu, W. Jiang, D. Zhang, J. Liang, Visible-light-driven photocatalytic degradation of diclofenac by carbon quantum dots modified porous g-C_3N_4: mechanisms, degradation pathway and DFT calculation, Water Res. 151 (2018) 8–19.
[48] X. Miao, Z. Ji, J. Wu, X. Shen, J. Wang, L. Kong, M. Liu, C. Song, g-C_3N_4/AgBr nanocomposite decorated with carbon dots as a highly efficient visible-light-driven photocatalyst, J. Colloid Interface Sci. 502 (2017) 24–32.
[49] C. Zhou, D. Huang, P. Xu, G. Zeng, J. Huang, T. Shi, C. Lai, C. Zhang, M. Cheng, Y. Lu, A. Duan, W. Xiong, M. Zhou, Efficient visible light driven degradation of sulfamethazine and tetracycline by salicylic acid modified polymeric carbon nitride via charge transfer, Chem. Eng. J. 370 (2019) 1077–1086.
[50] L. Jiang, X. Yuan, G. Zeng, Z. Wu, J. Liang, X. Chen, L. Leng, H. Wang, H. Wang, Metal-free efficient photocatalyst for stable visible-light photocatalytic degradation of refractory pollutant, Appl. Catal. B: Environ. 221 (2018) 715–725.
[51] Y. Wu, H. Wang, Y. Sun, T. Xiao, W. Tu, X. Yuan, G. Zeng, S. Li, J.W. Chew, Photogenerated charge transfer via interfacial internal electric field for significantly improved photocatalysis in direct Z-scheme oxygen-doped carbon nitrogen/CoAl-layered double hydroxide heterojunction, Appl. Catal. B: Environ. 227 (2018) 530–540.
[52] H. Wang, X. Yuan, Y. Wu, G. Zeng, X. Chen, L. Leng, H. Li, Synthesis and applications of novel graphitic carbon nitride/metal-organic frameworks mesoporous photocatalyst for dyes removal, Appl. Catal. B: Environ. 174–175 (2015) 445–454.
[53] H. Wang, Y. Bian, J. Hu, L. Dai, Highly crystalline sulfur-doped carbon nitride as photocatalyst for efficient visible-light hydrogen generation, Appl. Catal. B: Environ. 238 (2018) 592–598.
[54] Q. Liu, T. Chen, Y. Guo, Z. Zhang, X. Fang, Ultrathin g-C_3N_4 nanosheets coupled with carbon nanodots as 2D/0D composites for efficient photocatalytic H_2 evolution, Appl. Catal. B: Environ. 193 (2016) 248–258.
[55] K. Li, F.-Y. Su, W.-D. Zhang, Modification of g-C_3N_4 nanosheets by carbon quantum dots for highly efficient photocatalytic generation of hydrogen, Appl. Surf. Sci. 375 (2016) 110–117.
[56] M. Wu, J. Zhang, B.-B. He, H.-W. Wang, R. Wang, Y.-S. Gong, In-situ construction of coral-like porous P-doped g-C_3N_4 tubes with hybrid 1D/2D architecture and high efficient photocatalytic hydrogen evolution, Appl. Catal. B: Environ. 241 (2019) 159–166.
[57] Z. Xie, Y. Feng, F. Wang, D. Chen, Q. Zhang, Y. Zeng, W. Lv, G. Liu, Construction of carbon dots modified MoO_3/g-C_3N_4 Z-scheme photocatalyst with enhanced visible-light photocatalytic activity for the degradation of tetracycline, Appl. Catal. B: Environ. 229 (2018) 96–104.
[58] W.-J. Ong, L.K. Putri, Y.-C. Tan, L.-L. Tan, N. Li, Y.H. Ng, X. Wen, S.-P. Chai, Unravelling charge carrier dynamics in protonated g-C_3N_4 interfaced with carbon nanodots as co-catalysts toward enhanced photocatalytic CO_2 reduction: a combined experimental and first-principles DFT study, Nano Res. 10 (2017) 1673–1696.
[59] C. Zhou, C. Lai, D. Huang, G. Zeng, C. Zhang, M. Cheng, L. Hu, J. Wan, W. Xiong, M. Wen, X. Wen, L. Qin, Highly porous carbon nitride by supramolecular preassembly of monomers for photocatalytic removal of sulfamethazine under visible light driven, Appl. Catal. B: Environ. 220 (2018) 202–210.
[60] Y. Yang, Z. Zeng, C. Zhang, D. Huang, G. Zeng, R. Xiao, C. Lai, C. Zhou, H. Guo, W. Xue, M. Cheng, W. Wang, J. Wang, Construction of iodine vacancy-rich BiOI/Ag@AgI Z-scheme heterojunction photocatalysts for visible-light-driven tetracycline degradation: transformation pathways and mechanism insight, Chem. Eng. J. 349 (2018) 808–821.
[61] J. Cao, Z.-H. Yang, W.-P. Xiong, Y.-Y. Zhou, Y.-R. Peng, X. Li, C.-Y. Zhou, R. Xu, Y.-R. Zhang, One-step synthesis of Co-doped UiO-66 nanoparticle with enhanced removal efficiency of tetracycline: simultaneous adsorption and photocatalysis, Chem. Eng. J. 353 (2018) 126–137.
[62] F. Wang, P. Chen, Y. Feng, Z. Xie, Y. Liu, Y. Su, Q. Zhang, Y. Wang, K. Yao, W. Lv, G. Liu, Facile synthesis of N-doped carbon dots/g-C_3N_4 photocatalyst with enhanced visible-light photocatalytic activity for the degradation of indomethacin, Appl. Catal. B: Environ. 207 (2017) 103–113.
[63] X. Tang, G. Zeng, C. Fan, M. Zhou, L. Tang, J. Zhu, J. Wan, D. Huang, M. Chen, P. Xu, C. Zhang, Y. Lu, W. Xiong, Chromosomal expression of CadR on Pseudomonas aeruginosa for the removal of Cd(II) from aqueous solutions, Sci. Total Environ. 636 (2018) 1355–1361.
[64] D.L. Guan, C.G. Niu, X.J. Wen, H. Guo, C.H. Deng, G.M. Zeng, Enhanced *Escherichia coli* inactivation and oxytetracycline hydrochloride degradation by a Z-scheme silver iodide decorated bismuth vanadate nanocomposite under visible light irradiation, J. Colloid Interface Sci. 512 (2018) 272–281.
[65] G. Li, X. Nie, J. Chen, Q. Jiang, T. An, P.K. Wong, H. Zhang, H. Zhao, H. Yamashita, Enhanced visible-light-driven photocatalytic inactivation of *Escherichia coli* using g-C_3N_4/TiO_2 hybrid photocatalyst synthesized using a hydrothermal-calcination approach, Water Res. 86 (2015) 17–24.
[66] J. Liang, C. Shan, X. Zhang, M. Tong, Bactericidal mechanism of BiOI–AgI under visible light irradiation, Chem. Eng. J. 279 (2015) 277–285.
[67] W. Wang, J.C. Yu, D. Xia, P.K. Wong, Y. Li, Graphene and g-C_3N_4 nanosheets cowrapped elemental alpha-sulfur as a novel metal-free heterojunction photocatalyst for bacterial inactivation under visible-light, Environ. Sci. Technol. 47 (2013) 8724–8732.
[68] D. Xia, W. Wang, R. Yin, Z. Jiang, T. An, G. Li, H. Zhao, P.K. Wong, Enhanced photocatalytic inactivation of *Escherichia coli* by a novel Z-scheme g-C_3N_4/m-Bi_2O_4 hybrid photocatalyst under visible light: the role of reactive oxygen species, Appl. Catal. B: Environ. 214 (2017) 23–33.
[69] T. Wang, Z. Jiang, T. An, G. Li, H. Zhao, P.K. Wong, Enhanced visible-light-driven photocatalytic bacterial inactivation by ultrathin carbon-coated magnetic cobalt ferrite nanoparticles, Environ. Sci. Technol. 52 (2018) 4774–4784.
[70] J. Liang, F. Liu, M. Li, W. Liu, M. Tong, Facile synthesis of magnetic Fe_3O_4@BiOI@AgI for water decontamination with visible light irradiation: different mechanisms for different organic pollutants degradation and bacterial disinfection, Water Res. 137 (2018) 120–129.
[71] M. Cheng, Y. Liu, D. Huang, C. Lai, G. Zeng, J. Huang, Z. Liu, C. Zhang, C. Zhou, L. Qin, W. Xiong, H. Yi, Y. Yang, Prussian blue analogue derived magnetic Cu-Fe oxide as a recyclable photo-Fenton catalyst for the efficient removal of sulfamethazine at near neutral pH values, Chem. Eng. J. 362 (2019) 865–876.